Ultra-Low Thermal Conductivity in Nanoscale, Epitaxial SnS Grains

Michael Rohde,[1,2,3] Alessandra Canetta,[1] Yubin Huang,[1] Philip S. Dobson,[4] Jonathan M. R. Weaver,[4] Clement Merckling,[2,3] Francisco Molina-Lopez,[2] Jean Spiece,[1] and Pascal Gehring[1]

[1)] *Institute of Condensed Matter and Nanosciences, Université Catholique de Louvain (UCLouvain), 1348 Louvain-la-Neuve, Belgium*

[2)] *Department of Material Engineering,KU Leuven, 3001 Leuven, Belgium*

[3)] *IMEC, 3001 Leuven, Belgium*

[4)] *James Watt School of Engineering, University of Glasgow, Glasgow, G12 8LT, United Kingdom*

(*Electronic mail: pascal.gehring@uclouvain.be)

(Dated: 24 November 2025)

Thermally insulating nanoscale building blocks enable efficient routes to both passive and active heat management in miniaturized architectures. However, identifying suitable nano materials by computational and experimental means is difficult as critical dimensions reach the scale of thermal carriers and thermal interfaces become dominant. In this work, we propose epitaxially grown layered SnS as an outstanding thermal insulator at the thin film limit. The challenge of measuring heat transport at the nanoscale was tackled by locally probing out-of-plane thermal transport on grains of varying thickness utilizing scanning thermal microscopy. We consistently find an ultra-low thermal conductivity value of 45 $\mathrm{mWm^{-1}K^{-1}}$ which is among the lowest reported for dense solids to date. This finding challenges previous predictions of the SnS system and opens up promising prospects for its integration into heat management components.

The ongoing increase in computational density and energy consumption is accompanied by an increasing demand for efficient heat management at the nanoscale either by passive routes such as thermal insulation/channelling and waste heat recycling or by active routes such as thermoelectric cooling. Passive approaches critically depend on the availability of materials with low thermal conductivity k. Also active approaches benefit from low k as the thermoelectric figure of merit $zT = \sigma T S^2/k$ (where T is temperature, σ is the electrical conductivity and S is the Seebeck coefficient) inversely scales with k, making decreasing k a cornerstone for both passive and active thermal management technologies.

Tin mono sulfide (SnS) has attracted interest in the fields of ferroelectrics, photoabsorbers and thermoelectrics.[1–4]. SnS grows in an orthorhombic crystal structure analogous to phosphorene, featuring a combination of high S (400-700 μV/K), moderate electrical conductivity (0.1-1 S/m, depending on structure and doping), a low k (0.45-0.7 $\mathrm{Wm^{-1}K^{-1}}$ at room temperature) and a high degree of anisotropy with out-of-plane (OOP) stacked quasi van der Waals (vdW) layers and two anisotropic in-plane directions (see Fig.1(a))[2,5–8]. As a consequence of this anisotropy, thermal conductivity k is expected to differ significantly along the diverse crystallographic directions in SnS and especially between the in-plane and OOP directions[9].

Nevertheless, as with other anisotropic materials, SnS is often characterized globally as accessing the transport along different crystal axes is complicated, especially at the nanoscale. In this regime, critical dimensions reach the scale of the mean-free-path of thermal carriers (electrons and phonons) and thermal interfaces become dominant[10]. Additionally, approaching the nanoscale raises challenges in (at relevant scale) uniform material synthesis and ambient stability. Hence, overcoming these challenges in thermal characterization of nanoscale, anisotropic systems requires ideally local, non-invasive and consistent methods.

The Scanning Thermal Microscopy (SThM) method meets the demands for non-invasive nanoscale characterization, offering high spatial resolution and thermal sensitivity but suffering somewhat from a set of tip-sample interactions which complicate quantitative interpretations. The feasibility of SThM for characterizing thermal transport in 2D materials and the closely related SnSe system has previously been reported[11–14]. On SnS, however, such studies have been absent in the literature.

In this work, we demonstrate nanoscale characterization of thermal transport in ultra-thin, highly crystalline SnS grains epitaxially grown on c-plane α-Al_2O_3. We use SThM to locally measure the thermal resistance of crystallographically aligned SnS grains, revealing an ultra low effective thermal conductivity, one order of magnitude lower than in bulk SnS. We attribute this finding to strain induced inter-planar disorder of AB stacked SnS layers which can suppress thermal transport as previously reported in other vdW materials[15,16]. Our findings are consolidated by using multiple calibration method approaches for the thermal probes, ensuring statistically significant results. With its ultra-low thermal conductivity, SnS shows great potential for heat management applications, paving the way for boosted efficiency by integrating thin SnS films into thermal devices.

SnS thin films were grown on commercial 2" c-plane α-Al_2O_3 wafers by plasma-assisted molecular beam epitaxy. The base pressure of the growth chamber was 10^{-9} Torr. The as-delivered wafer was pretreated by heating from the back of the substrate up to a T set point of 750 °C and exposure to H_2S plasma from a radio frequency (RF) source with a power of 600 W and resulting in a temporary chamber pressure of 10^{-5} Torr. After 10 minutes pre-treatment, the sample was left to cool to growth temperature (set point 350 °C). The film was grown by simultaneous exposure to 100 W RF H_2S plasma and Sn vapor from an effusion cell kept at 1130 °C. For the reference sample, 300 nm of SiO_2 were thermally grown on bulk Si. The variation of SiO_2 thickness was achieved through

an inclined cut by a focused ion beam.

To determine the crystal structure of the SnS thin film, we performed high-angle annular dark field scanning transmission microscopy (HAADF-STEM) and X-ray diffraction (XRD). A good match between the characteristic stacking of the SnS layers (a-face) with the HAADF-STEM image of a 18 nm thick grain is shown in Fig.1(b). The XRD spectrum in Fig.1(c) shows exclusively two peaks matching to OOP directions SnS(004) and SnS(008) which confirms the global alignment of SnS grains. We observe small deviations from theoretical 2θ values, which we attribute to crystallographic strain. An additional confirmation of the SnS phase is provided by the Raman spectrum shown in Fig.1(d)(i). Five of the most prominent modes at 95.0 cm^{-1}, 187.4 cm^{-1}, 220.0 cm^{-1}, 158.7 cm^{-1} and 135.1 cm^{-1} can be attributed to the $A_{g(1-3)}$ and a double set of B_g modes, respectively[17]. Next, we consider the edge of the as-grown SnS thin film, where average grain thickness is gradually decreased and the amount of exposed substrate gradually increases. Fig.1(d)(ii) shows Raman spectra recorded along a 40 μm long line across this transitional area (marked green in the optical image). We find a transition between saturated signal at x=0 μm to completely vanished signal at x=40 μm. Notably, the major Raman peaks from Fig.1(d)(i) decrease equally across the full 40 μm until vanishing (see Supplementary Material, Fig. S1) and without the appearance of any further Raman peaks. Hence, we conclude that the SnS phase remains pure across the edge transition.

To characterize the thermal conductivity, we recorded SThM data within the transitional area of the SnS film edge, making use of the gradual variation of material thickness. Fig.2(a) shows a topographic map of the SnS films edge region (see also Fig.2(b)), transitioning from an almost continuous coverage with roughly 20 nm high SnS grains on the left to a region with sparse coverage with only few nm high, dendritic SnS shreds and a high amount of substrate exposure. Subsections of this map contain a varying distribution of grain thickness while the lateral scale of the grains remains similar. In Fig.2(c), we show a schematic of the thermal transport measurement which allows simultaneous recording of topography and thermal voltage U_{SThM}. U_{SThM} is a measure of the cool-down of the heated probe caused by varying thermal conductance through the tip-sample interface which depends on both, interface and material properties. Maps of topography and U_{SThM} are shown in Fig.2(d). The topographic and thermal voltage maps were recorded using a Bruker Icon Dimension scanning probe platform with a commercially available SThM probe (KNT-SThM-2an, Kelvin Nanotechnology) under an ambient environment. The thermal voltage signal was amplified and read out by the lock-in technique (operated at 91 kHz) coupled to a Wheatstone bridge as reported elsewhere[12,18]. Due to the thermalization time of the probe ($\approx$ 1 ms), the heating remains effectively constant at this frequency, depending only on the DC part of the applied current. The thermal response (i.e. $R_{\mathrm{el}}(T)$, where R_{el} is the electrical probe resistance and T is temperature) was calibrated prior to

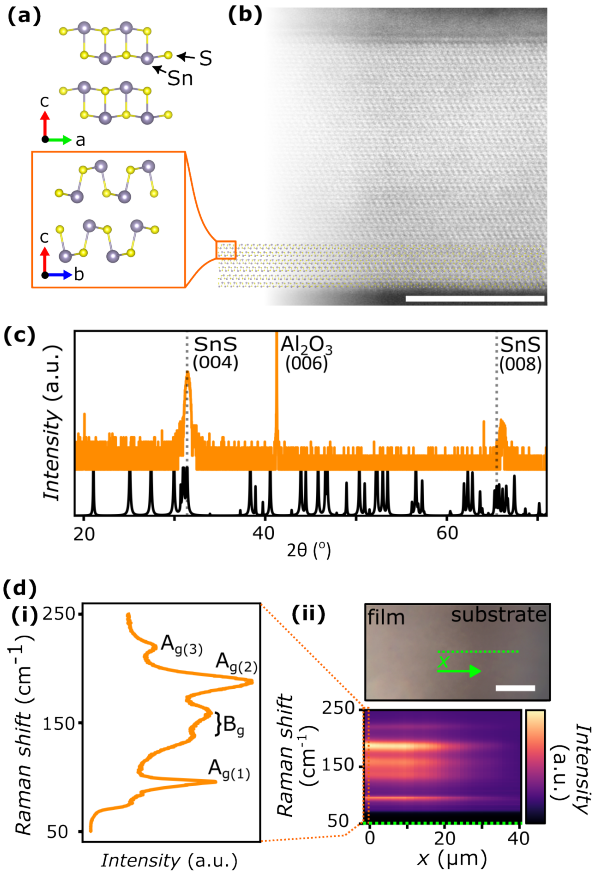

FIG. 1. (a) b-face and a-face of SnS. (b) Overlay of a-face SnS model with HAADF-STEM image of a SnS grain. Scale bar is 10 nm. (c) Out-of-plane XRD scan of SnS thin film (orange) and theoretical XRD spectrum (black, computed using VESTA software). (d) (i) Raman spectrum on the SnS thin film and (ii) across the transition at the edge of the film. The substrate is Raman silent in the displayed range (first peak at 417 cm^{-1}). The scale bar in the image is 20 μm.

measurements as explained elsewhere[12].

To obtain the thermal resistance R_{th} from U_{SThM}, we calibrated the probe by recording point traces (Fig.2(e)) on the α-Al_2O_3 substrate (thermal conductivity of α-Al_2O_3[19]: $k_{Al_2O_3}$=35 $Wm^{-1}K^{-1}$). In such a point trace, the change in U_{SThM} is measured while the distance between probe and surface is gradually decreased beyond contact. Using this calibration effectively compares the recorded U_{SThM} signal to ΔU_{SThM} from when the tip is in full thermal contact with the substrate and when the tip is thermally out of contact. This ΔU_{SThM} depends on the specifics of the probe and the thermal conductivity of the substrate (see also Supplementary Material, Fig. S2). The thermal resistance R_{th} measured by the SThM method comprises several components in series[13,18]: the tip thermal resistance R_{tip}, the tip-sample interface resistance R_{int} and the heat spreading resistance R_{S}. For a given material, R_{tip} and R_{int} can be considered constant, leaving only R_{S} to vary with sample thickness h. Fig.2(f) shows a histogram representation of all values computed from the images in Fig.2(d). Here, constant contributions have been subtracted

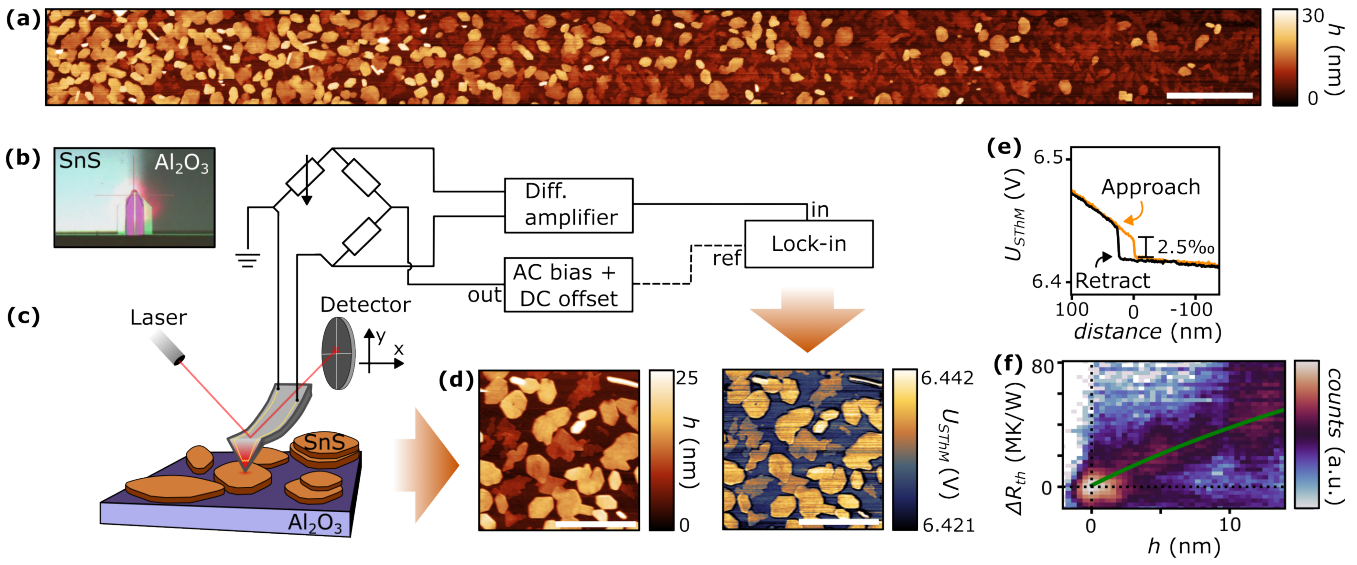

FIG. 2. SThM across the edge of a SnS thin film on α-Al_2O_3. (a) Topographic map of the transition from continuous SnS film to isolated SnS grains. Scale bar is 2 μm. (b) Optical image of the SThM probe scanning the edge of the SnS film. (c) Schematic of SThM measurement as detailed in the main text. (d) Topographic and SThM signal U_{SThM} map of SnS grains in an area with balanced thickness h distribution. Scale bars are 1 μm. (e) Approach curve taken on the α-Al_2O_3 substrate. The distance on the x-axis is defined as the tip-substrate separation. (f) Histogram of ΔR_{th} VS grain thickness h of SnS. Data outside dotted lines are due to a small variation of measured substrate signal (at $h < 0$ nm) and artifacts from short loss of thermal contact (visible as shadow in U_{SThM} map in (d) leading to data at $\Delta R_{\mathrm{th}} < 0$ MK/W) and have been excluded from the fit (green line).

in $\Delta R_{\mathrm{th}} = R_{\mathrm{S}}(h) - R_{\mathrm{S},0}$, where $R_{\mathrm{S},0}$ is the thermal resistance measured at $h = 0$ nm. Thus, the variation in ΔR_{th} in Fig.2(f) arises only from the thickness variation of the SnS grains. We fit $\Delta R_{\mathrm{th}}(h)$ with $R_{\mathrm{S}}(h)$ (green line in Fig.2(f)) using a model developed in previous works[18,20];

$$R_{\mathrm{S}}(h) = \frac{1}{\pi k_1 a_{\mathrm{eff}}} \int_0^\infty \left[\frac{1 + K \exp\left(-\frac{2\xi h_{\mathrm{eff}}}{a_{\mathrm{eff}}}\right)}{1 - K \exp\left(-\frac{2\xi h_{\mathrm{eff}}}{a_{\mathrm{eff}}}\right)} \right] J_1(\xi) \sin(\xi) \frac{d\xi}{\xi^2} \tag{1}$$

, where a_{eff} is the radius of the effective thermal contact area, h_{eff}=h + r_{int} x k_1 is an effective thickness including the layer-substrate interfacial resistance (r_{int}) and effective thermal conductivity of the material layer (k_1), J_1 is the first-order Bessel function of the first kind and the K parameter is defined as

$$K = \frac{1 - \frac{k_s}{k_1}}{1 + \frac{k_s}{k_1}} \tag{2}$$

where k_{S} is the thermal conductivity of the substrate. We obtain ultra-low values of order $k_1 \approx 10^{-2}$ $\mathrm{Wm^{-1}K^{-1}}$ for the thin SnS grains (more details below, see Fig.4(a)). Here, the effective contact area has been approximated based on line traces in the topographic map (see Supplementary Material, Fig. S3 and S4).

To substantiate our finding of ultra-low thermal conductivity further, we performed a complementary approach (dataset B) for the approximation of the effective tip radius. In Fig.3, we present dataset B recorded using another SThM probe and a SiO_2/Si reference sample. Fig.3(a) shows a schematic of the reference measurement; thermal resistance variation is achieved through thickness variation by an inclined cut through a 300 nm SiO_2 layer as reported elsewhere[18]. Fig.3(b) shows topographic and U_{SThM} maps recorded on the reference sample represented by a ΔR_{th} vs thickness h histogram in Fig.3(c). Using the known thermal conductivity of SiO_2, k_{SiO_2}=1.3 - 1.4 $\mathrm{Wm^{-1}K^{-1}}$, we fit R_{S} and extract a_{eff}= 74.1 - 88.5 nm. In analogy to Fig.2(d) and (f), Fig.3(d) and (e) show topographic and U_{SThM} maps of an area semi-populated by SnS grains of various heights and a histogram of ΔR_{th} VS SnS thickness (see Supplementary Material, Fig. S2 for corresponding substrate approach curves). Using a_{eff} from this

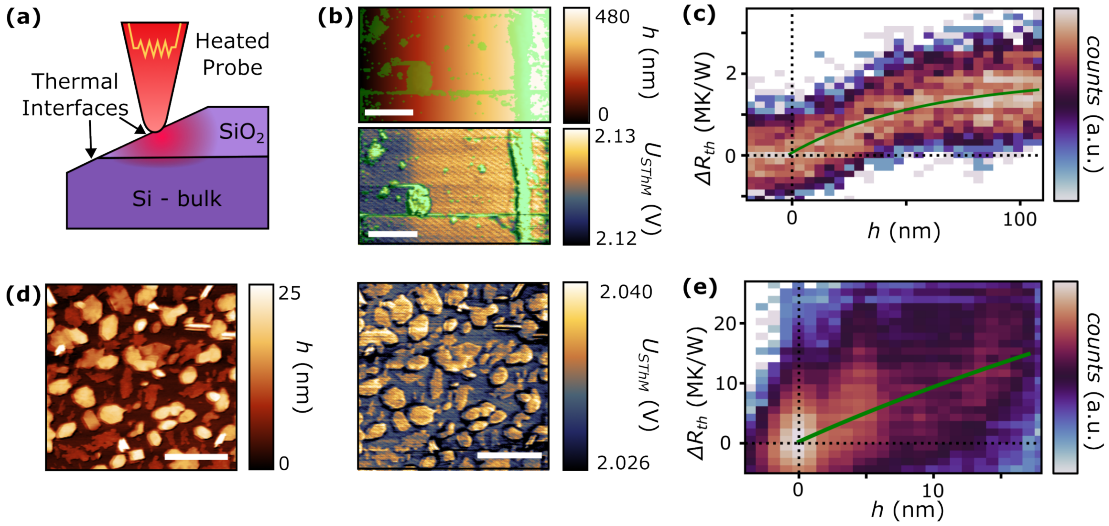

FIG. 3. SThM dataset B including a SiO_2/Si reference. (a) Schematic of reference measurement. (b) Topographic and U_{SThM} maps of the SiO_2/Si reference. Contamination on the sample surface are marked in green and excluded from analysis. (c) Histogram of ΔR_{th} VS grain thickness h of SiO_2/Si. Dotted lines indicate the data thresholds for the fit. (d) Topography and U_{SThM} maps of SnS grains. (e) Histogram of ΔR_{th} VS grain thickness h of SnS. As before, dotted lines indicate the thresholds of data inclusion for the fit (green line). All scale bars in the maps are 1 μm.

calibration to again fit R_{S} likewise returns an ultra-low SnS thermal conductivity of the order of 10^{-2} $\mathrm{Wm^{-1}K^{-1}}$.

The effective SnS thermal conductivity k_{SnS} extracted from the fits crucially depends on the estimate of the effective thermal contact area, i.e. the contact radius a_{eff}. Fig.4(a) shows k_{SnS} resulting from fits to both datasets with varying assumed values of the a_{eff} parameter. The probes of dataset A and B have significantly different a_{eff} but produce a qualitatively and, within experimental error bar, quantitatively consistent k_{SnS}. Combining both datasets by weighted average yields an ultra low value of k_{SnS}=45 $\pm$ 7 $\mathrm{mWm^{-1}K^{-1}}$, one order of magnitude lower than the value range 0.45-0.7 $\mathrm{Wm^{-1}K^{-1}}$ of bulk SnS at room temperature[2,5–7] and amongst the lowest reported in solid materials to date (see Fig.4(b)).

The horizontal error bars in Fig.4(a) represent estimates for a_{eff}. In case of dataset A, the error is a combination of line trace variation and uncertainty about the real width of the grain edges (see Supporting Material, Fig. S3). In the case of dataset B, the error contains variation of approach curves, uncertainty about the exact SiO_2 thermal conductivity, and the possible formation of a water meniscus between tip and thin film, which can contribute an estimated 6% to the flow of heat[21]. Dataset A and B are consistent within error estimates. At the same time, these findings highlight the need and challenge to accurately estimate a_{eff}. We find that the use of a calibration sample (dataset B) is providing a significantly improved accuracy compared to the common method of estimating a_{eff} by topographic line-traces (dataset A), which is particularly prone to variation of topographic line traces and edge-sharpness related overestimates of the effective thermal contact radius (see Supporting Material, Fig. S4). Further sources of error that may lead to an underestimate in our analysis such as the effect of lateral thermal penetration depth and additional thermal interfaces due to grain overlap have been excluded in our analysis (see Supporting Material, Fig. S5 for more detail).

Concerning the ultra-low value of thermal conductivity; three key factors contributing to low thermal conductivity in SnS have been identified in previous studies; low intrinsic thermal conductivity (low phonon velocity, high phonon scattering probability), SnS phase ($k_{\mathrm{cubic}} < k_{\mathrm{orthorhombic}}$) and transport direction (c-axis is the hard axis, i.e. has lowest thermal conductivity)[24–26]. Indeed, vdW materials naturally host the potential for large thermal anisotropy[16,25]. We note that our measurement geometry applies a temperature gradient along the OOP axis (i.e., c-axis) and the film thickness is small compared to the thermal contact radius (i.e. h / a_{eff} << 1). Thus, the measured thermal resistance predominately reflects the OOP thermal transport in the grains. This assessment is further supported by finite element modeling (see Supporting Material, Fig. S6). Nevertheless, a thermal conductivity as low as in the present study occurs rarely in dense solids. Ultra-low cross-plane thermal conductivities, especially compared to their bulk counterparts, have been measured by time-domain thermoreflectance on WSe_2, WS_2 and MoS_2 thin films with interlayer disorder[15,16]. In analogy to the materials in these studies, the observed strain in our SnS film (Fig.1(c)) likely promotes the ultra-low thermal conductivity in multiple ways; by altering phonon transport intrinsically as previously reported in other thin film materials[27,28] and with dopant induced strain in SnS[29], and by inducing inter-planar stacking

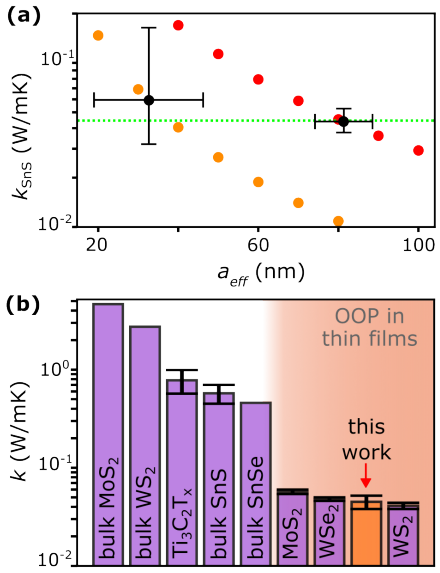

FIG. 4. Comparison of k_{SnS} from both datasets with literature. (a) shows k_{SnS} extracted from the model depending on the tip radius parameter a_{eff} for datasets A (orange) and B (red). Estimated a_{eff} are represented by the error bars an estimated average values by black points. The weighted average of k_{SnS}=45 $mWm^{-1}K^{-1}$ (standard deviation ± 7 $mWm^{-1}K^{-1}$) is represented by the green dotted line. (b) Comparison of k_{SnS} from this work with out-of-plane thermal conductivity of other vdW materials in literature: bulk WS_2 and MoS_2[22], highly conductive $Ti_3C_2T_x$ flakes[12], bulk SnS[2,5–7] bulk SnSe[23], and thin film MoS_2, WS_2[15] and WSe_2[15] with interlayer disorder.

variation leading to impeded inter-layer phonon transport.

The potential of simultaneously tuning electrical conductivity and, via the hypothetical link with strain, the thermal conductivity by doping, points out the significant prospects for the design of thermoelectrics and thermal rectifiers or resonators based on thin film SnS. At present, the already ultra-low thermal conductivity observed in this study makes this material a high potential ingredient in components for multiple applications such as photo absorber layers, thermal insulators and active thermoelectric materials, all of which benefit from the spatial retention of heat flows.

In summary, we measured the out-of-plane thermal conductivity of SnS by a local probing method that utilizes thickness variation of grains at a film transition area. We report two datasets, each with a different approach for determining the effective thermal contact area between the SThM probe and the material, a parameter that crucially impacts the modeling of the thin film thermal conductivity. The two approaches vary in accuracy but consistently yield an ultra-low thermal conductivity value k_{SnS}=45 $\pm$ 7 $mWm^{-1}K^{-1}$ which is among the lowest reported for dense solids to date. This finding highlights the exceptional potential of SnS based building blocks for heat management and outlines the progression of nanoscale thermal insulation based on vdW layered materials.

SUPPLEMENTARY MATERIAL

The supplementary material contains further Raman analysis, SThM approach curves, elaboration on tip radius estimates, a closer inspection of individual grains and finite element modeling.

The authors acknowledge financial support from the F.R.S.-FNRS of Belgium (FNRS-CQ-1.C044.21-SMARD, FNRS-CDR-J.0068.21-SMARD, FNRS-MIS-F.4523.22-TopoBrain, FNRS-PDR-T.0128.24-ART-MULTI, FNRS-CR-1.B.463.22-MouleFrits, FNRS-FRIA-1.E092.23-TOTEM, FNRS-GEQ-UG.0102.2F-Attohmics), from the EU (ERC-StG-10104144-MOUNTAIN), from the Fédération Wallonie-Bruxelles through the ARC Grant No. 21/26-116, and from the FWO and FRS-FNRS under the Excellence of Science (EOS) programme (40007563-CONNECT) and by KU Leuven Internal Funds Global PhD Partnerships with UC Louvain (GPUCL/21/021).

The authors have no conflicts to disclose. Data that support the findings of this study are available from the corresponding author upon reasonable request.

REFERENCES

[1]Asfandiyar, W. Xue, J. Mao, K. Liu, Q. Zhang, J.-F. Li, *ACS Applied Materials & Interfaces* **2024**, *16*, 29 38073.
[2]Q. Tan, L.-D. Zhao, J.-F. Li, C.-F. Wu, T.-R. Wei, Z.-B. Xing, M. G. Kanatzidis, *Journal of Materials Chemistry A* **2014**, *2*, 41 17302.
[3]H. Öztürk, F. Aslan, *Optical Materials* **2022**, *131* 112755.
[4]N. Higashitarumizu, H. Kawamoto, C.-J. Lee, B.-H. Lin, F.-H. Chu, I. Yonemori, T. Nishimura, K. Wakabayashi, W.-H. Chang, K. Nagashio, *Nature communications* **2020**, *11*, 1 2428.
[5]B. Zhou, S. Li, W. Li, J. Li, X. Zhang, S. Lin, Z. Chen, Y. Pei, *ACS applied materials & interfaces* **2017**, *9*, 39 34033.
[6]Y.-M. Han, J. Zhao, M. Zhou, X.-X. Jiang, H.-Q. Leng, L.-F. Li, *Journal of Materials Chemistry A* **2015**, *3*, 8 4555.
[7]J. Prado-Gonjal, J. Gainza, I. Aguayo, Ó. J. Durá, S. Rodríguez-Pérez, F. Serrano-Sánchez, N. M. Nemes, M. T. Fernández-Díaz, J. A. Alonso, E. Morán, *Materials Advances* **2020**, *1*, 4 845.
[8]S. Gedi, V. R. Minnam Reddy, T. R. R. Kotte, C. Park, W. K. Kim, *nanomaterials* **2021**, *11*, 8 1955.
[9]R. Guo, X. Wang, Y. Kuang, B. Huang, *Physical Review B* **2015**, *92*, 11 115202.
[10]S. Chatterjee, Paras, H. Hu, M. Chakraborty, *Processes* **2023**, *11*, 9 2769.
[11]M. Ozdogan, T. Iken, D. Cakir, N. Oncel, *Applied Physics Letters* **2024**, *125*, 24.
[12]Y. Huang, J. Spiece, T. Parker, A. Lee, Y. Gogotsi, P. Gehring, *ACS nano* **2024**, *18*, 47 32491.
[13]J. Spiece, S. Sangtarash, M. Mucientes, A. J. Molina-Mendoza, K. Lulla, T. Mueller, O. Kolosov, H. Sadeghi, C. Evangeli, *Nanoscale* **2022**, *14*, 7 2593.
[14]S. Gonzalez-Munoz, K. Agarwal, E. G. Castanon, Z. R. Kudrynskyi, Z. D. Kovalyuk, J. Spièce, O. Kazakova, A. Patanè, O. V. Kolosov, *Advanced Materials Interfaces* **2023**, *10*, 17 2300081.
[15]C. Chiritescu, D. G. Cahill, N. Nguyen, D. Johnson, A. Bodapati, P. Keblinski, P. Zschack, *Science* **2007**, *315*, 5810 351.
[16]S. E. Kim, F. Mujid, A. Rai, F. Eriksson, J. Suh, P. Poddar, A. Ray, C. Park, E. Fransson, Y. Zhong, D. A. Muller, P. Erhart, D. G. Cahill, J. Park, *Nature* **2021**, *597*, 7878 660.

[17]P. Sutter, H. Komsa, H. Lu, A. Gruverman, E. Sutter, *Nano Today* **2021**, *37* 101082.
[18]J. Spièce, C. Evangeli, A. J. Robson, A. El Sachat, L. Haenel, M. I. Alonso, M. Garriga, B. J. Robinson, M. Oehme, J. Schulze, F. Alzina, C. S. Torres, O. V. Kolosov, *Nanoscale* **2021**, *13*, 24 10829.
[19]R. L. Aggarwal, A. K. Ramdas, *Physical properties of diamond and sapphire*, CRC Press, **2019**.
[20]Y. Muzychka, M. Yovanovich, J. Culham, *Journal of thermophysics and heat transfer* **2004**, *18*, 1 45.
[21]A. Assy, S. Gomès, *Nanotechnology* **2015**, *26*, 35 355401.
[22]P. Jiang, X. Qian, X. Gu, R. Yang, *Advanced Materials* **2017**, *29*, 36 1701068.
[23]L.-D. Zhao, S.-H. Lo, Y. Zhang, H. Sun, G. Tan, C. Uher, C. Wolverton, V. P. Dravid, M. G. Kanatzidis, *nature* **2014**, *508*, 7496 373.
[24]J. M. Flitcroft, I. Pallikara, J. M. Skelton, *Solids* **2022**, *3*, 1 155.
[25]J. Li, T. Yan, X. Gong, H. Zou, B. Zhang, H. Wu, G. Wang, X. Zhou, *The Journal of Physical Chemistry Letters* **2023**, *14*, 33 7346.
[26]M. Zhang, I. Pallikara, J. M. Flitcroft, J. M. Skelton, *Journal of Materials Chemistry A* **2025**.
[27]M. Alam, M. P. Manoharan, M. A. Haque, C. Muratore, A. Voevodin, *Journal of Micromechanics and Microengineering* **2012**, *22*, 4 045001.
[28]X. Zhang, G. Wu, *Journal of Nanomaterials* **2016**, *2016*, 1 4984230.
[29]P. Krishna, V. Vijay, S. Ponnusamy, M. Navaneethan, *CrystEngComm* **2024**, *26*, 40 5767.

Supporting Material for: Ultra-Low Thermal Conductivity in Nanoscale, Epitaxial SnS Grains

FURTHER RAMAN ANALYSIS

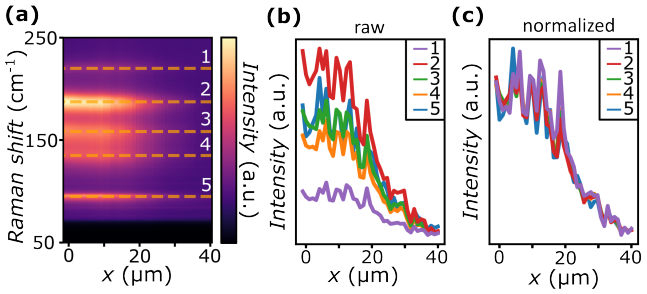

FIG. S1. Further Raman analysis. (a) Shows Raman spectra mapped across the edge of the SnS film. Major peak positions are marked and labeled 1-5. (b) Peak intensities along lines marked in a). (c) Normalized peak intensities showing equal behavior of all major peaks.

STHM APPROACH CURVES ON SUBSTRATES

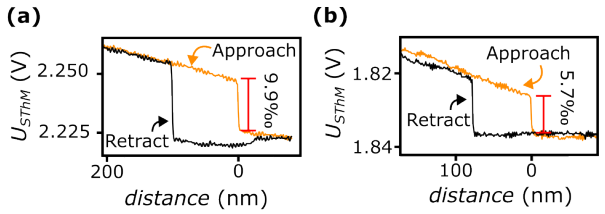

FIG. S2. Approach curves recorded on (a) Si and (b) Al_2O_3 for dataset B in main text. The same probe yields more variation on the Si substrate due to its higher thermal conductivity.

TIP RADIUS ESTIMATE

As discussed in the main text, the effective radius a_{eff} of the thermal contact area plays a crucial role in the analysis of scanning thermal microscopy (SThM) data. Here, we discuss two potential sources of error on a_{eff} in more detail: omitting the finite slope of grain edges (here modeled as straight slopes) and the overestimate of the contribution of the physical tip radius a_{tip} to the effective radius for thermal transport a_{eff}. Fig.S3 illustrates the former potential source of error coming into play when

$$b_{\text{real}} < b' = \frac{2b_{\text{meas}}}{1-b_{\text{meas}}^2}, \tag{S1}$$

where $b_{\text{real}} = \Delta h/\Delta w_{\text{real}}$, $b_{\text{meas}} = \Delta h/\Delta w_{\text{meas}}$ are the real and measured slope of the grain edges, respectively. Given b_{real}, this relation provides a quantifiable threshold useful for assessing whether the grain edge slope can be neglected. In Fig.S4 (a) and (b) we estimate a lower limit for b_{real} from a high resolution tapping-mode AFM image taken on the more continuous part of the film. We obtain $b_{\text{real}} \geq 1.28$. In Fig.S4c), we compare b' in Eqn.S1 (computed for profiles 1-9 across grain edges in topographic data in Fig.S4(d)(i)) to this lower limit. We find the condition is not met for any of the measured grain edges. Consequently, using model 1, we obtain $a_{\text{tip}} = (58.2 \pm 24.8)$ nm.

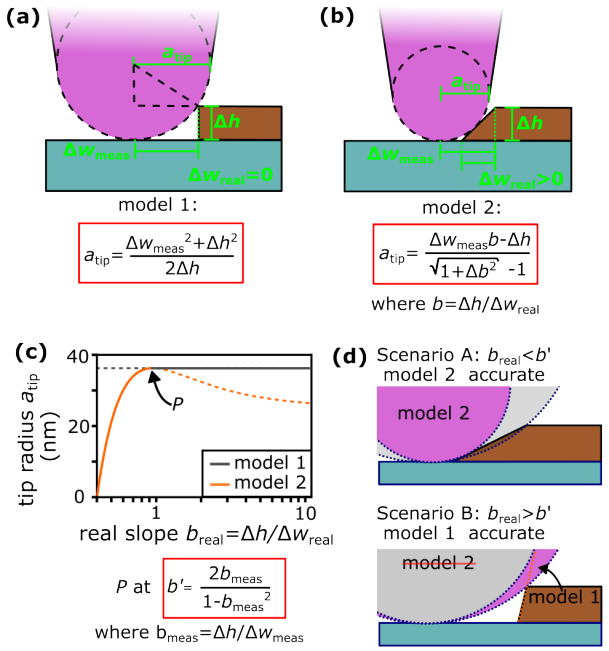

FIG. S3. Illustration of edge slope impact on the estimate of tip radius a_{tip}. (a) and (b) show idealized cases for when the grain's slope may or may not be omitted leading to model 1 and model 2, respectively . (c) demonstrates the error for a given scenario with b_{meas}=0.4; for $b_{\text{real}} < b'_{\text{real}}$ model 1 overestimates a_{tip} and model 2 is accurate and vice versa. d) shows both scenarios for the exemplary case of b_{meas}=0.4.

To estimate the contribution of the physical tip radius a_{tip} to the effective thermal contact radius a_{eff}, we compare the aforementioned topographic profiles 1-9 to their corresponding counterparts in the SThM signal (Fig.S4(d)(i) and (ii) and e)). The widths of the SThM profile steps are consistently smaller than the width of the corresponding topographic steps by an average factor $c = 0.72$. Factoring in this correction into our measurement of topographic width w in our estimate from model 1 finally yields $a_{\text{eff}} = (32.7 \pm 13.9)$ *nm*.

CLOSER INSPECTION OF INDIVIDUAL GRAINS

We assess the impact of lateral thermal penetration depth on our analysis by checking for U_{SThM} variation along the lateral dimensions of the grains. Fig.S5 shows line traces along the scan direction crossing the lateral dimensions of seven dif-

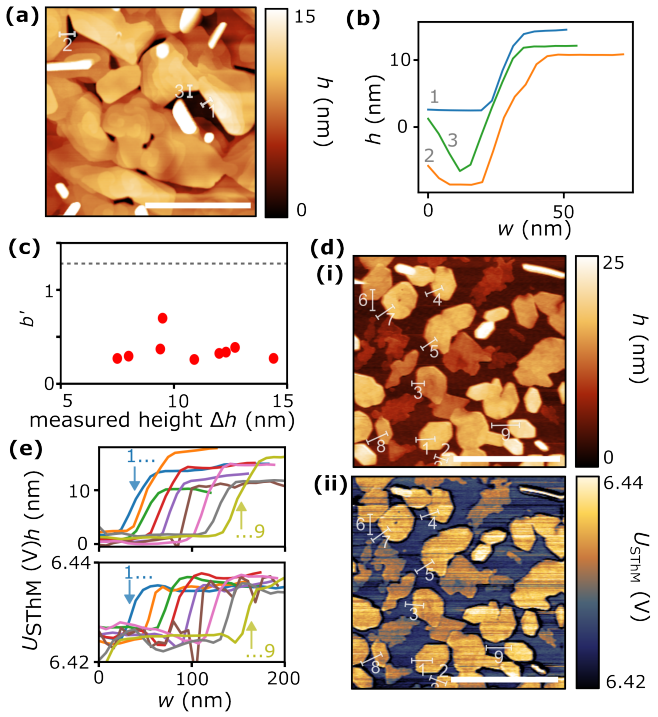

FIG. S4. Topographic and SThM data for the estimate of a_{eff}. (a) High resolution tapping-mode AFM of semi-continuous part of SnS film. (b) Profiles extracted from edges in (a). (c) b' extracted from topographic profiles in (d)(i). The dotted line represents the lower limit estimate of b_{real} extracted from (b). (d) Topographic and SThM signal maps. Indicated profile lines correspond to profiles in (e) (labelled 1-9 from left to right). Scale bars in all images are 1 μm.

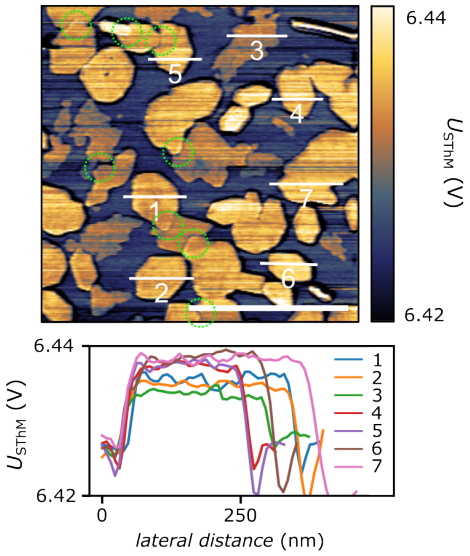

FIG. S5. Closer inspection of individual grains on the U_{SThM} map from Fig.2(d) for assessing artificial contributions to k_{SnS}. Line profiles are flat along lateral dimension of 7 assessed grains. Grain overlap regions are marked by green dotted circles. Scale bar is 1 μm.

ferent grains. We find no significant difference between central and edge regions of SnS grains. Additionally, interfaces formed between overlapping SnS grains may locally decrease U_{SThM} decreasing the value of k_{SnS}. However, we find no significant impact of this effect in such regions (highlighted in Fig.S5).

FINITE ELEMENT MODELING

We performed finite element modeling to assess the impact of the lateral boundaries on the thermal spreading resistance. We model the grain with a fixed thickness of 20 nm, resting on an alumina substrate and vary the grain radius. The substrate is a square of 10 µm lateral size. The SThM tip is modeled as a circular heat source on the grain surface. To determine the thermal spreading resistance, we compute the average temperature rise in the circle and normalize to the power injected, as $R_{\text{th}} = \mathrm{d}T/Q$. We performed the simulations for the two tip contact radii used in the experiments (32 nm and 74 nm). The results are shown in Fig. S6(a). It can be observed that the grain radius only has a marginal effect on thermal resistance.

Next, by systematically changing the in-plane and out-of-plane thermal conductivity of the grain, we obtained a thermal resistance heatmap to study the impact of the anisotropy. For both, a 10 nm (Fig. S6(b)(i)) and a 20 nm (Fig. S6(b)(ii)) thick grain, it can be observed that the in-plane thermal conductivity (horizontal axis) has less impact on the measured thermal resistance than the out-of-plane thermal conductivity (vertical axis).

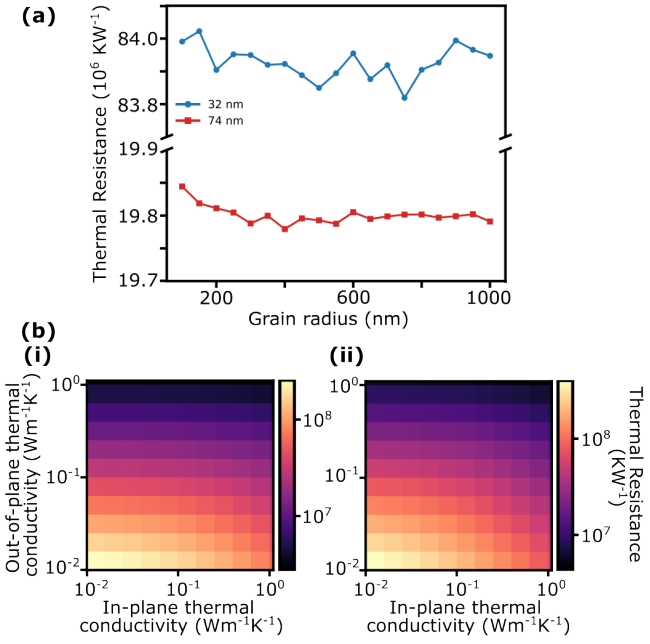

FIG. S6. Finite element modeling of the grain radius impact (a) and thermal conductivity anisotropy (b) on the thermal spreading resistance. In (a), two contact radii are used, as in the experiment. In (b), the results are shown for a 10 nm (i) and a 20 nm (ii) thick grain.